JGR Space Physics

RESEARCH ARTICLE
10.1029/2025JA033912

# Concurrent GOLD and SABER Observations of Thermosphere Composition and Temperature Responses to the April 23–24, 2023 Geomagnetic Storm

**Xuguang Cai[1], Wenbin Wang[2], Richard W. Eastes[1], Liying Qian[2], Martin G. Mlynczak[3], J. S. Evans[4], Ningchao Wang[3], Nabil Nowak[3], Nicholas Pedatella[2], and Kun Wu[2]**

[1]Laboratory of Atmospheric and Space Physics, University of Colorado, Boulder, CO, USA, [2]High Altitude Observatory, National Center for Atmospheric Research, Boulder, CO, USA, [3]Langley Research Center, NASA, Hampton, VA, USA, [4]Computational Physics, Inc., Springfield, VA, USA

**Abstract** The Global-scale Observations of Limb and Disk (GOLD) and Sounding of the Atmosphere using Broadband Emission Radiometry (SABER) instruments were used to investigate the thermospheric composition and temperature responses to the geomagnetic storm on 23–24 April, 2023. Global-scale Observations of Limb and Disk observed a faster recovery of thermospheric column density ratio of O to $N_2$ ($\Sigma O/N_2$) in the southern hemisphere (SH) after the storm ended at 12 Universal time (UT) on 24 April. After 12 UT on 25 April, $\Sigma O/N_2$ had mostly recovered in both hemispheres. Global-scale Observations of Limb and Disk also observed an increase of middle thermospheric temperature (140–200 km) (Tdisk) on 24 April with a maximum of 340 K. Within 4–6 hr of the storm ending on 24 April, Tdisk enhancement persisted between 30°N and 60°N, 100°W and 30°W, while Tdisk lower than pre-storm quiet day (17 April) was observed between 45°W and 15°W, 40°S and 50°N. Tdisk recovered between 100°W and 45°W, 30°N and 55°S. On 25 April, Tdisk was lower than on 17 April across the entire GOLD Field-of-Regard (FOR) by ~50–110 K. Additionally, solar irradiance decreased by 15%–20% from 17 to 25 April, indicating that the lower Tdisk on 25 April resulted from both storm and solar irradiance variations. Latitudinal variations of Tdisk and the SABER observed Nitric Oxide (NO) cooling rate revealed that NO cooling is crucial for the lower Tdisk in the northern hemisphere (NH) mid-high latitudes on 25 April. These results provide direct evidence of decreased thermospheric temperature during storm recovery phase than pre-storm quiet times.

**Plain Language Summary** Geomagnetic storms strongly impact thermosphere composition and temperature. In this paper, we reported thermospheric composition and temperature responses to a strong geomagnetic storm using data measured by the Global-scale Observations of the Limb and Disk mission in a geostationary orbit and the SABER instrument onboard a low-earth-orbiting satellite. After the storm ended at 12 UT on 24 April, the thermospheric column density ratio of O to $N_2$ ($\Sigma O/N_2$) recovered faster in the SH. $\Sigma O/N_2$ mostly recovered in both hemispheres on 25 April. Global-scale Observations of Limb and Disk observed maximum storm-time temperature enhancements of 340 K in the middle thermosphere (140–200 km). However, the temperature is lower on 25 April than that on the quiet day before the storm by 50–110 K. Latitudinal variations of temperature perturbations after the storm suggest that NO cooling rate, which is measured by the SABER instrument, makes crucial contributions to the lower temperature in the recovery phase in the mid-high latitudes of the NH. In summary, our study provides direct evidence of post-storm, lower temperature in the middle thermosphere.

**Key Points:**

- After the 23–24 April, 2023 storm ended, $\Sigma O/N_2$ depletion recovers faster in the southern hemisphere than in the northern
- Northern hemisphere (NH) mid-latitude temperature on 25 April (the day after the storm) is 50–110 K lower than the one before the storm (17 April)
- Nitric Oxide cooling plays a crucial role in causing the lower post-storm temperature in the NH mid-high latitudes on 25 April

**Supporting Information:**

Supporting Information may be found in the online version of this article.

**Correspondence to:**

X. Cai,
xuca8770@colorado.edu

**Citation:**

Cai, X., Wang, W., Eastes, R. W., Qian, L., Mlynczak, M. G., Evans, J. S., et al. (2025). Concurrent GOLD and SABER observations of thermosphere composition and temperature responses to the april 23–24, 2023 geomagnetic storm. *Journal of Geophysical Research: Space Physics*, *130*, e2025JA033912. https://doi.org/10.1029/2025JA033912

Received 12 MAR 2025
Accepted 5 APR 2025

**Author Contributions:**

**Conceptualization:** Xuguang Cai
**Data curation:** Xuguang Cai
**Funding acquisition:** Xuguang Cai, Wenbin Wang, Richard W. Eastes
**Investigation:** Xuguang Cai
**Methodology:** Xuguang Cai
**Project administration:** Wenbin Wang, Richard W. Eastes
**Visualization:** Xuguang Cai, Nabil Nowak
**Writing – original draft:** Xuguang Cai
**Writing – review & editing:** Xuguang Cai, Wenbin Wang, Richard W. Eastes, Liying Qian, Martin G. Mlynczak, J. S. Evans, Ningchao Wang, Nicholas Pedatella, Kun Wu



## 1. Introduction

The responses of thermospheric composition to geomagnetic disturbances have been extensively studied for several decades (Burns et al., 1989; Prölss, 2011). Based on the observations from satellite-borne mass spectrometer and numerical modeling, Prölss (2011) summarized how thermospheric composition responds to geomagnetic storms. After the onset of a storm, high-latitude Joule heating is greatly enhanced which leads to variations in temperature, temperature gradients, and wind divergence or convergence in the polar region, causing neutral composition disturbances through upwelling or downwelling. The polar composition disturbances near local midnight are then transported equatorward to mid and even low latitudes by the storm-enhanced, equatorward winds. As Prölss (2011) pointed out, this effect "is most pronounced in the longitude sector containing the magnetic poles." The composition disturbances also corotate from local mid-night into the local morning sector

and daytime to be observed by space-borne airglow imagers (Eastes et al., 2017; Paxton et al., 1999). In addition, the recovery time of the mid and high-latitudes thermosphere composition disturbances range from 12 hr to 1 day (Burns et al., 1989; Yu, Wang, et al., 2022). The classical theory mentioned above has been validated by numerous studies (e.g., Burns et al., 1995; Cai et al., 2021, 2023, 2024; Fuller-Rowell et al., 1994; Yu et al., 2021; Yu, Cai, et al., 2022, 2023; Yu, Wang, et al., 2023).

Thermospheric temperature is a key parameter in space weather research and application. It not only illustrates the energy budget of the thermosphere, but also impacts winds and thermospheric mass density to modulate satellite drag force. Obtaining and understanding the temperature profile across the entire thermosphere are therefore essential. However, most previous studies focused on the impact of storms on neutral temperature in the upper thermosphere (200–500 km; Lei et al., 2011, 2012; Li et al., 2024, 2025) or in the mesosphere and lower thermosphere (80–110 km; Liu et al., 2018; Li et al., 2018; Wang et al., 2021; Pancheva et al., 2007; Yuan et al., 2015). There have been very few studies on middle thermosphere (140–200 km) temperature due to a lack of neutral temperature observations. Although Aksnes et al. (2006) proposed to utilize the $N_2$ Lyman-Birge-Hopfield (LBH) retrievals to measure temperature in the middle thermosphere, published results on temperature behavior in this region remain limited. According to Burns et al. (1992), the thermospheric temperature enhancement in the high latitudes during storm-time is primarily due to Joule heating. In contrast, the temperature enhancement in the mid-latitudes results mainly from compressional heating. Additionally, NO cooling, which is greatly increased during storms with enhanced auroral precipitation, plays a major role in reducing storm-time temperature to regulate the thermosphere energy budget (Burns et al., 1995; Knipp et al., 2013, 2017; Lei et al., 2012; Mlynczak et al., 2003; Sheng et al., 2017; Verkhoglyadova et al., 2014, 2017). Lei et al. (2012) found that for a storm in October 2003, the post-storm temperature derived from neutral mass density was lower than the one on the pre-storm quiet day. They attributed this "overcooling" phenomenon to the large post-storm NO cooling rates observed by Sounding of the Atmosphere using Broadband Emission Radiometry (SABER) onboard the Thermosphere Ionosphere Mesosphere Energetics and Dynamics (TIMED) satellite. Zhang et al. (2019) argued that the overcooling is also impacted by the changes in solar irradiance during that event. Note that most previous studies used neutral mass density measurements, which is sensitive to both composition and temperature. Furthermore, there has been no direct observational evidence of a decreased thermospheric temperature after a storm.

Two-dimensional (2D) synoptic imaging of $\sum O/N_2$ and disk temperature (Tdisk) from the Global-scale Observations of the Limb and Disk (GOLD) mission in geo-stationary orbit enables the investigation of middle thermosphere (140–200 km) composition and temperature responses to geomagnetic storms, which provides direct evidence of composition and temperature evolution during and after the storm. In this paper, we report the 2D temporal evolution of $\sum O/N_2$ and Tdisk responses to a $Kp = 8^+$ major geomagnetic storm that occurred from DOY 113 to 115 (23 to 25 April) in 2023 (Aa et al., 2024). Sounding of the Atmosphere using Broadband Emission Radiometry observations of NO cooling rates are used to understand post-storm Tdisk variations. The remainder of this paper is organized as follows. Section 2 describes the data. Section 3 provides results. Section 4 gives the discussion, and the conclusions are presented in Section 5.

## 2. Data

### 2.1. GOLD Data

The GOLD is onboard the SES-14 communication satellite (launched on 25 January 2018) in a geostationary orbit over 47.5°W. Global-scale Observations of Limb and Disk provides Far-Ultraviolet spectrum airglow images of the same geographic region (60°S–60°N, 120°W–20°E) in a similar universal time (UT) range (06:10–00:25 UT of the next day) every day. It observes Earth's airglow emissions from 134 to ∼162 nm, including the OI 135.6 nm and $N_2$ LBH during the daytime (8:10–18:10 UT, 2 hr interval) (Eastes et al., 2020). $\sum O/N_2$ is derived from the daytime OI 135.6 nm and $N_2$ LBH brightness (Correira et al., 2021; Evans et al., 1995; Strickland et al., 1995). The Tdisk is derived from the $N_2$ LBH band widths, most of which comes from within one scale height of 150 km (Evans et al., 2024). In this study, we use the GOLD observed $\sum O/N_2$ (version 4.0) and Tdisk (version 5.0) in both hemispheres with a spatial resolution of $2° \times 2°$. During 2023 April, the uncertainty of the $\sum O/N_2$ data are 5%–10% (Correira et al., 2021). The uncertainties of Tdisk at each pixel are ∼20–80 K (3%–8% of Tdisk, Evans et al., 2024). Additionally, GOLD observations of $Q_{EUV}$, a proxy for the integrated solar EUV irradiance 1–45 nm, are also utilized (Correira et al., 2021; Evans et al., 1995; Strickland et al., 1995, 2004). The daily mean of $Q_{EUV}$ is used to describe the solar irradiance variations.

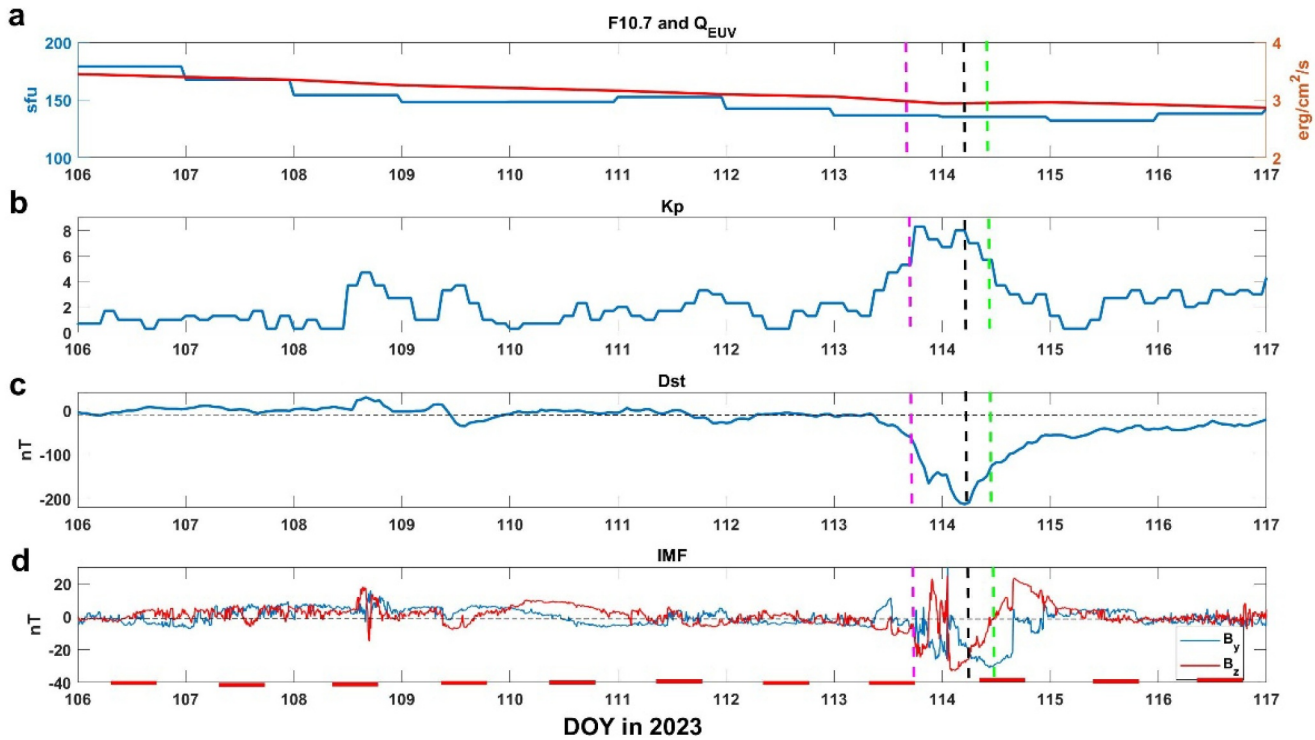


**Figure 1.** Temporal variations of (a) F10.7 and Global-scale Observations of Limb and Disk (GOLD) observed solar $Q_{EUV}$, (b) Kp, (c) Dst, and (d) Interplanetary Magnetic Field $B_y$ and $B_z$ from DOY 106 to DOY 116 in 2023. The red part in *X* axis in each day stands for the observation period of GOLD. The pink dotted line stands for the beginning of the storm main phase. The black dotted line marks the starting of recovery phase. The green line marks the ending of storm.

### 2.2. SABER NO Cooling Rate

The SABER instrument is on-board the NASA TIMED satellite, which was launched on 7 December 2001 into a 74.1° inclination orbit at ~630 km altitude (Esplin et al., 2023; Russell et al., 1999). The SABER infrared sensor performs about 1,400 radiance limb scans a day, in 10 distinct spectral channels from 1.27 to 15.4 μm (Mlynczak, 1997; Mlynczak et al., 2005, 2007), including NO infrared emission at 5.3 μm, which is used to derive the NO cooling rate (Mlynczak et al., 2010, 2021). The latitude coverage of the SABER instrument shifts between 83°N and 53°S and 53°N–83°S every 60 days due to the satellite yaw cycle. The latitude coverage from DOY 113 to 116 in 2023 is between 83°N and 53°S. The data version of NO cooling rate we use in this paper is version 2.0. The systematic error is 3%, and the random error is $5.8 \times 10^{-11}$ W/m$^3$ (Wang et al., 2024).

## 3. Results

### 3.1. Geomagnetic Conditions

Figure 1 shows (a) F10.7 and GOLD observed Qeuv, (b) the Kp index, (c) the disturbance storm (Dst) index and (d) Interplanetary Magnetic Field (IMF) north-south component ($B_z$) and east-west component ($B_y$) between DOY 106 and 116. F10.7 decreased from 167 sfu on DOY 106 to 132 sfu on DOY 116. Daily mean Qeuv varied from 3.4/erg/cm$^2$/s on DOY 106 to 2.8/erg/cm$^2$/s on DOY 116. On DOY 106 and 107, Kp mostly remained below 2. Kp jumped from $1^+$ at 6 UT on DOY 113 to $8^+$ at 18 UT on DOY 113 and to 8 at 3 UT on DOY 114. It then gradually decreased until 6 UT on DOY 115 with a Kp value of less than 1. Dst was more positive than −30 nT before DOY 113, dropping to −215 nT at 5 UT on DOY 114 before rebounding to ~−30 nT at the end of DOY 115. IMF $B_z$ was mostly southward (−32.8 nT) after 2:50 UT on DOY 114, turned to northward (positive) after 12 UT on DOY 114 and stayed northward until 12:30 UT on DOY 115. IMF $B_y$ reached −31 nT at 10 UT on DOY 114, shifting to positive (eastward) after 22 UT on DOY 114. Based on geomagnetic indices, DOY 107 was selected as the quiet reference day. The storm commenced around 18 UT on DOY 113 (marked by the pink dotted line) and the recovery phase began at 5 UT on DOY 114 (marked by black dotted line). Note that even after the beginning of recovery phase, there are still significant magnetospheric energy inputs to the thermosphere.

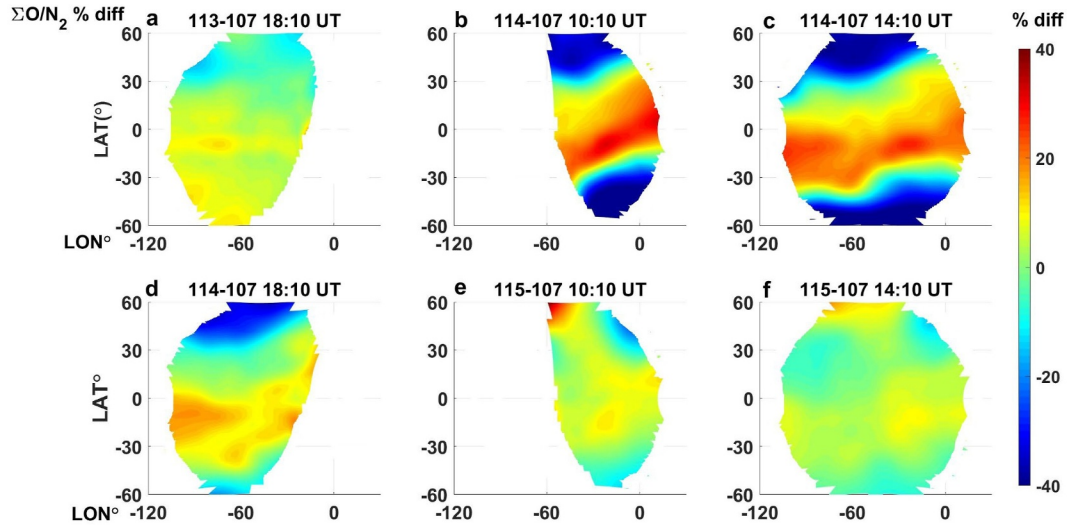


**Figure 2.** Percentage difference of Global-scale Observations of Limb and Disk observed $\Sigma O/N_2$ between (a) DOY 113 at 18:10 Universal time (UT), (b)–(d) 114 at 10:10, 14:10, and (e)–(f) 115 at 10:10, 14:10 UT and 107.

Therefore, we define the end of storm as the time when $B_z$ turned northward (12 UT on DOY 114, marked by the green dotted line).

### 3.2. Thermospheric Composition and Temperature Variations During and After the Storm

Figures 2a–2f show the geographic latitude-longitude distribution of the percentage difference in $\sum O/N_2$ between DOY 113 (23 April) to 115 (25 April) and DOY 107 (17 April). The percentage difference is calculated by subtracting $\sum O/N_2$ on the quiet day from the one on the disturbed day and then divided by $\sum O/N_2$ on the quiet day to illustrate the relative variations of $\sum O/N_2$ during disturbed times. A "depletion (enhancement)" stands for a negative (positive) percentage difference to indicate smaller (larger) $\sum O/N_2$ on the disturbed day than on the quiet reference day. Temporal evolution of $\sum O/N_2$ variation is shown in movie S1. At 18:10 UT on DOY 113 (Figure 2a, storm main phase), $\sum O/N_2$ depletion (15%) appears between 30°N and 50°N, 100°W and 75°W. No significant variations occur in other areas within the GOLD FOR. At 10:10 UT on DOY 114 (Figure 2b, recovery phase but before the storm ending), the northern hemisphere (NH) $\sum O/N_2$ depletion extends more equatorward (to 30°N) in western longitudes in the GOLD FOR (closer to NH magnetic pole) with a maximum magnitude of 42%. In the southern hemisphere (SH), the $\sum O/N_2$ depletion penetrates to 15°S–35°S with a maximum magnitude of 46% and more equatorward in the eastern longitudes (closer to SH magnetic pole). A stronger $\sum O/N_2$ enhancement occurs in the SH lower geographic latitudes than in the NH. At 14:10 UT (recovery phase and 2 hr after the storm ending, Figure 2c), the equatorward boundary of NH $\sum O/N_2$ depletion between 50°W and 10°W is similar to that at 10:10 UT, while the SH depletion between 30°W and 0°E retreats to higher latitudes (30°S–45°S). At 18:10 UT on DOY 114 (recovery phase and 6 hr after the storm ending, Figure 2d), the NH $\sum O/N_2$ depletion persists with a magnitude of 30% in the north of 30°N. However, SH high-latitude depletion decays and shrinks to the south of 50°S. At lower latitudes, the SH $\sum O/N_2$ enhancement continues to exist with a maximum magnitude of 18% between 0°S and 30°S, 110°W and 30°W. $\sum O/N_2$ in other areas within the GOLD FOR mostly recovered (percentage difference < 10%). Movie S1 illustrates that the SH $\sum O/N_2$ enhancement still exists at 8:10 UT on DOY 115 with a maximum magnitude of 16% between 0 and 25°S, 20°W and 10°E. While depletion occurs in the east edge of GOLD FOR. At 10:10 UT on DOY 115, SH $\sum O/N_2$ enhancements decay to less than 10%. Northern hemisphere depletion mostly disappears within GOLD FOR. At 14:10 UT, magnitudes of $\sum O/N_2$ variations within the entire GOLD's FOR are below 8%, indicating a full recovery of $\sum O/N_2$.

Figures 3a–3f depict the differences GOLD Tdisk between DOY 113 to 115 and DOY 107. Temporal evolution of Tdisk variation is shown in Movie S2. After the storm commencement at 18:10 UT on DOY 113 (Figure 3a, beginning of the storm), Tdisk enhancement (a maximum of 105 K) occurs between 30°N and 60°N, 100°W and 45°W. In the SH, Tdisk enhancement appear between 70°W and 40°W, 50°S and 27°S with a maximum magnitude of 40 K. Some Tdisk reductions occur between 35°W and 15°W, 25°N and 50°N, and between 100°W

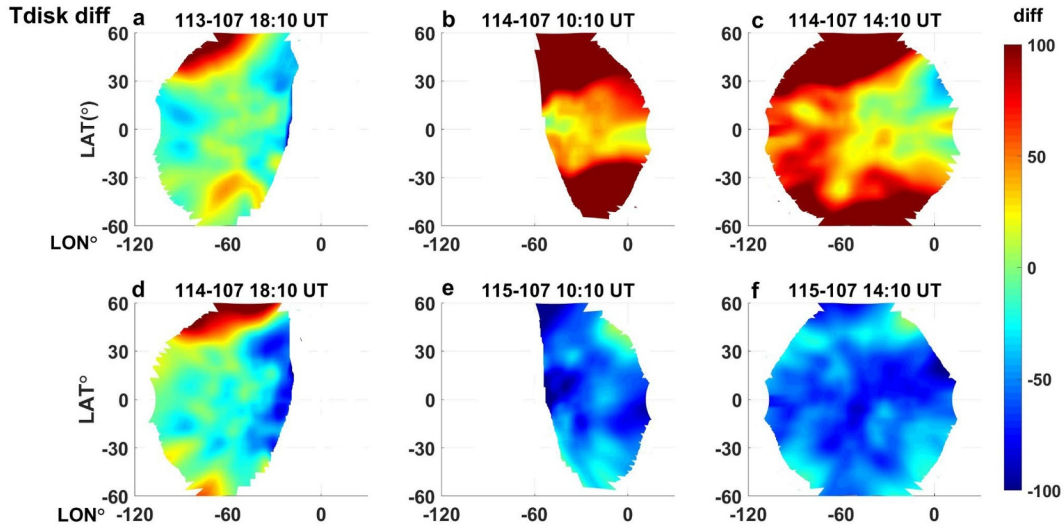


**Figure 3.** Difference of Global-scale Observations of Limb and Disk observed Tdisk between (a) DOY 113 at 18:10 Universal time (UT), (b)–(d) 114 at 10:10, 14:10, and (e)–(f) 115 at 10:10, 14:10 UT and 107.

and 80°W, 8°N and 15°N with a maximum magnitude of 50 K. No salient variations of Tdisk occur in other areas within the GOLD FOR. At 10:10 UT on DOY 114 (recovery phase but before storm ending, Figure 3b), Tdisk increases across the entire GOLD FOR, with the region overlapping with $\sum O/N_2$ depletion showing a maximum enhancement of 340 K. On the other hand, Tdisk enhancement corresponding to the $\sum O/N_2$ enhancement is smaller with a maximum of 90 K. Additionally, more Tdisk enhancements occur in the NH. For example, Tdisk enhancements over 300 K occur between 50°W and 0°E, 40°N and 60°N in the norther hemisphere (50° × 20°), while they only take place between 45°S and 60°S, 30°W and 20°W in the SH (15° × 10°). At 14:10 UT (recovery phase and 2 hr after the storm ending, Figure 3c), Tdisk mostly recovers (Tdisk difference < 40 K (~5%)) between 48°W and 15°E in the mid-low latitudes. The latitude range is larger on the east side of GOLD FOR (47°N–18°S) than towards the westside (20°N–12°S). Compared with Figure 3b (10:10 UT), Tdisk difference between 50°W and 0°E decreases ~60–80 K in the mid-low latitudes in 4 hr. Tdisk enhancement persists in the mid-high latitudes with more equatorward extension on the west side of GOLD FOR. However, the magnitude of enhancement decreases to 220 K in the NH and 170 K in the SH. The temporal evolution of Tdisk variations (Movie S2) shows that compared with Tdisk difference at 12:10 UT (when storm ends), Tdisk enhancement at 14:10 UT decreases 80 and 30 K in the mid-high latitudes of the northern and SH, respectively. At 18:10 UT (recovery phase and 6 hr after the storm ending, Figure 3d), Tdisk enhancement (40–90 K) occurs between 40°N and 60°N, 95°W and 25°W. Tdisk reduction (40–100 K) appears between 50°W and 20°W, 50°N to 45°S. Tdisk mostly recovers in other areas within the GOLD FOR. The temporal evolution of Tdisk variations (Movie S2) shows that Tdisk reduction on DOY 114 starts at 16:10 UT (recovery phase and 4 hr after the storm ending).

On DOY 115, Tdisk is lower at 8:10 UT (first daytime observation) than on DOY 107 (50–110 K) in the entire GOLD FOR. This, together with Figure 3d, indicates that Tdisk also decreases between 18:10 UT on DOY 114 and 8:10 UT on DOY 115. At 10:10 and 14:10 UT (Figures 3e and 3f), Tdisk on DOY 115 is also 50–110 K lower than the one on DOY 107.

In summary, during the storm time, the $\sum O/N_2$ depletion is stronger in NH western longitudes and in SH eastern longitudes. After the storm ends (12 UT on DOY 114), $\sum O/N_2$ depletion recovers faster in the SH. After 10 UT on DOY 115, $\sum O/N_2$ mostly recovers in both hemispheres. Tdisk increases by a maximum of 340 K during the storm with more enhancements in the NH within GOLD FOR. Tdisk enhancement decreases immediately after the storm ends at 12 UT on DOY 114 (as large as 80 K in 2 hr). Lower post-storm Tdisk than pre-storm quiet day (DOY 107, 17 April) appears after 4 hr of storm ending. It dominates the entire GOLD FOR on the second day (DOY 115) with a maximum magnitude of 110 K.

To better characterize the storm-induced Tdisk variations, latitudinal profiles of Tdisk differences between DOYs 114 to 116 and 107 at 20°W, 47.5°W and 62.5°W from 12:10 UT to 16:10 UT are shown in Figure 4. The bin size

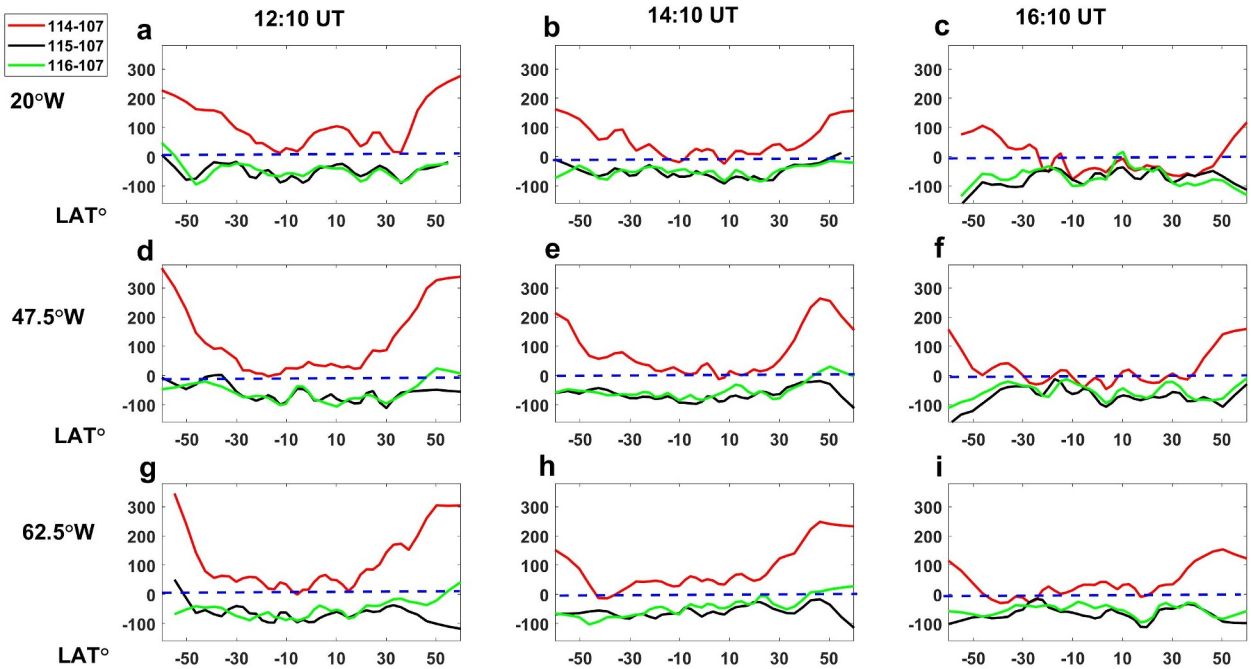


**Figure 4.** Latitudinal variations of Tdisk differences between DOY (blue) 114, (red) 115 (black) 116 and 107 at (a–c) 20°W, (d–f) 47.5°W, and (g–i) 62.5°W from 12:10 to 16:10 Universal time.

is 10°. DOY 116 is included because it has almost the same solar irradiance and geomagnetic condition as DOY 115, thus serving as the reference. The corresponding uncertainties of Tdisk differences (obtained by standard error propagation) are shown in Figure S1 in Supporting Information S1. As shown in Figure 4, during the early stage of the storm recovery phase and after the storm ending (12:10–16:10 UT on DOY 114, red line), the Tdisk enhancement is larger at mid-high latitudes with the magnitude decreasing towards the equator. The enhancement reaches 340 K in mid-high latitudes (25–60°N/S, uncertainties ∼25–60 K) and 100 K in low latitudes (25°S–25°N, uncertainties ∼20 K) at 12:10 UT (Figures 4a–4g). At 14:10 UT (recovery phase and 2 hr after the storm ending), Tdisk enhancements drop to 260 K in mid-high latitudes (25°–60°N/S, uncertainties ∼35–40 K) and 40 K in low latitudes (25°S–25°N, uncertainties ∼25 K) at 20°W (Figure 4b). At 47.5°W and 62.5°W (Figures 4e and 4h), the maximum Tdisk enhancements at mid-high latitudes (25°–60°N/S, uncertainties ∼25–45 K) and low latitudes (25°S–25°N, uncertainties ∼20 K) in the two hemispheres are 260 and 70 K, 190 and 80 K, respectively. Tdisk difference begins to become negative in some mid-low latitudes. At 16:10 UT (recovery phase and 4 hr after the storm ending), Tdisk difference between DOY 114 and 107 is negative with a maximum magnitude of 80 K between 20°S and 45°N at 20°W, −50 K between 30°S and 38°N at 47.5°W and −45 K between 45°S and 20°N at 62.5°W (uncertainties ∼20–30 K). Besides the negative Tdisk difference, the Tdisk enhancements reach a maximum of 105, 140 and 150 K at 20°W, 47.5°W and 62.5°W (uncertainties ∼25–50 K), respectively.

The Tdisk differences between DOY 115, 116 and DOY 107 are mostly negative (black and green lines in Figure 3) at these three longitudes and are similar between 45°S and 30°N (−100 to −10 K). However, at 12:10 and 14:10 UTs, 47.5°W, and 12:10 to 16:10 UT at 62.5°W, Tdisk differences between DOY 115 and 107 (black lines) are 50–100 K less than those between DOY 116 and 107 (green lines) in the NH mid-high latitudes (30–60°N). In the SH mid-high latitudes, a smaller difference (20–30 K) within the uncertainties (25–50 K) also appears, but only at 16:10 UT at these 3 longitudes.

### 3.3. NO Cooling Variations During and After the Storm

Figure 5 shows the UT and latitudinal variations of NO cooling rate observed by SABER at 120, 140 and 160 km. The data covers 6–10 local time (LT) (local morning, ascending, Figures 5a–5c) and 0–6 LT (local night, descending, Figures 5d–5f) from DOY 113 to the end of DOY 116 across all longitudes where the orbits pass. The two white lines mark when the main phases of the storm begin (18 UT on DOY 113) and when the storm ends (12

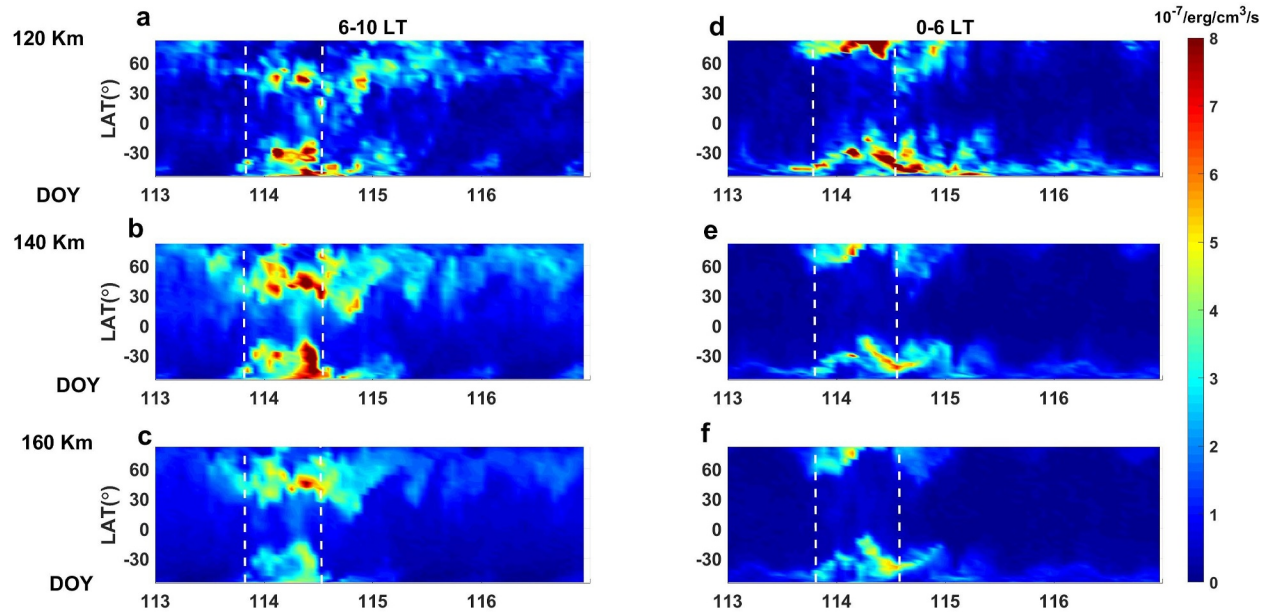


**Figure 5.** Universal time and latitudinal variations of Nitric Oxide cooling rate at local daytime and local nighttime from DOY 113 to 116 near (a–b) 120, (c–d) 140, and (e–f) 160 km. Two white lines stand for the beginning time of main and recovery phase.

UT on DOY 114). During the storm, the NO cooling rate between 6 and 10 LT increases from less than $2 \times 10^{-7}$/erg/cm$^3$/s to 6–8 $\times 10^{-7}$/erg/cm$^3$/s at these altitudes, especially in mid-latitudes (25–55°N/°S) (Figures 5a–5c). After the storm ends at 12 UT on DOY 114, NO cooling quickly decreases in the SH, but more slowly in the NH. On DOY 115, the NO cooling rate is still larger in the NH(1–3 $\times 10^{-7}$/erg/cm$^3$/s) than that in the SH (<1 $\times 10^{-7}$/erg/cm$^3$/s). During 0–6 LT (Figures 5d–5f), although NO cooling rate increases (from less than $2 \times 10^{-7}$/erg/cm$^3$/s to 6–8 $\times 10^{-7}$/erg/cm$^3$/s) during the storm, it decreases quickly after the storm. At 120 km, the post-storm NO cooling rate in the SH is larger than that in the NH.

Figure 5 presents a depiction of the temporal evolution of the latitudinal distribution of the NO cooling rate at different altitudes from the SABER measurements. To elucidate how the NO cooling rate evolves within the GOLD FOR during and after the storm, we select three UTs of Tdisk differences and overlay four SABER orbits where NO cooling rate measurements were taken as they passed through the GOLD FOR. Since the Tdisk difference reflects the cumulative effects of various heating and cooling processes, including NO cooling, the UTs of these orbits precede those of the Tdisk difference. The Tdisk differences for one UT are during the storm's main phase, while the other two are after the storm, on DOY 114 and 115, respectively.

Figure 6a shows the Tdisk difference between DOY 114 and 107 at 10:10 UT, with four SABER orbits overplotted. Each of these orbits corresponds to a time before 10:10 UT on DOY 114. The pink circle orbit overlaps with the GOLD FOR, covering latitudes 56°N to 49°S and longitudes 47°W to 3.6°W. This orbit corresponds to UT 3.4–3.9 (~3.7) on DOY 114. The plus sign orbit near the GOLD FOR stands for 5–5.5 (~5.3) UT and covers 58°N, 71°W to 49°S, 26°W. The star orbit (56°N, 95°W to 41°S, 6°W) represents 7.2–7.6 (~7.4) UT, and the Cross orbit (56°N, 8°E to 51°S, 49°W) stands for the 8.5–9.5 (~9) UT. Figure 6d depict the NO cooling rate values along these orbits at 160 km between 120°W and 30°E, 83°N and 51°S.As illustrated in Figure 6d, at 3.7 UT (circle sign), NO cooling rate at 160 km is slightly over $2 \times 10^{-7}$/erg/cm$^3$/s in the NH with the maximum ($2.6 \times 10^{-7}$/erg/cm$^3$/s) occurs near 45°N, 49°W. However, the NO cooling rate at SH is much larger than the NH (a maximum of $5.9 \times 10^{-7}$/erg/cm$^3$/s). At 5.3 UT (plus sign), the maximum NO cooling rate in the NH ($4 \times 10^{-7}$/erg/cm$^3$/s) occurs at 26°N, 49°W. At 7.4 UT (star sign), the maximum value in NH increases to $4.5 \times 10^{-7}$/erg/cm$^3$/s while still located near 26°N. At 9 UT (cross sign), NO cooling rate increases significantly, and its maximum value reaches $8.3 \times 10^{-7}$/erg/cm$^3$/s but its latitude changes to 45°N. In the SH, NO cooling rate $> 2 \times 10^{-7}$/erg/cm$^3$/s penetrates equatorward to 25°S. The observations along these four orbits indicate that NO cooling in the SH within the GOLD FOR responds to storm more quickly than in the NH (3.7 UT on DOY 114).

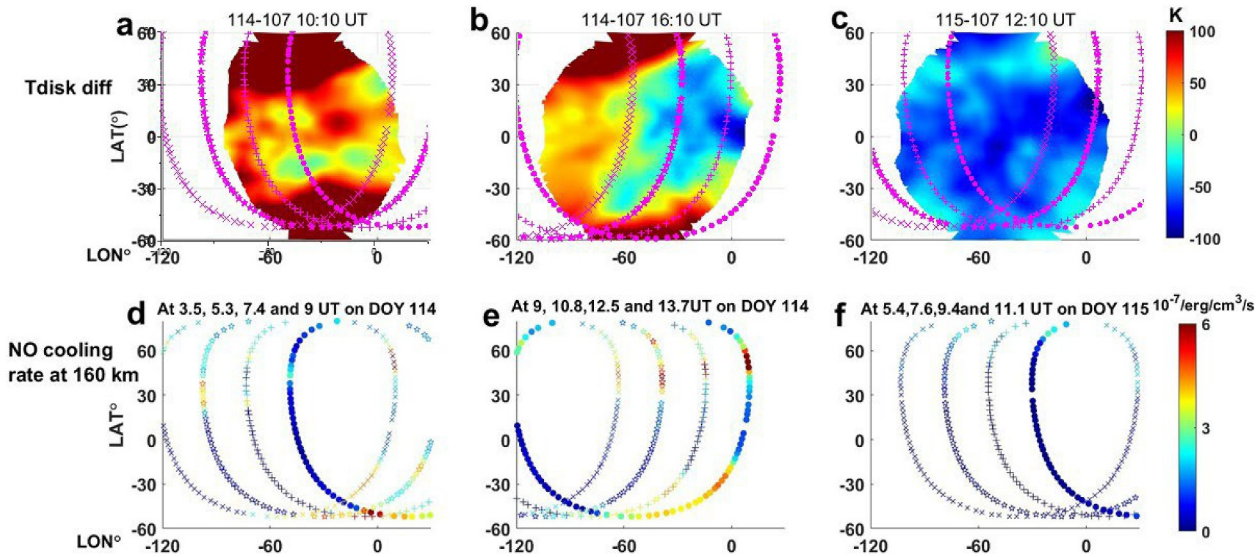


**Figure 6.** Tdisk difference between DOY 107 and 114 at (a) 10:10 Universal time (UT), (b) 16:10 UT. (c) Tdisk between DOY 115 and 107 at 12:10 UT overplotted with four Sounding of the Atmosphere using Broadband Emission Radiometry orbits. The circle, plus, star and cross stand for orbits near (a) 3.7, 5.3, 7.4 and 9 UT on DOY 114, (b) 9, 10.8, 12.5 and 13.7 UT on DOY 114, (c) 5.5, 7.6, 9.4 and 11.1 UT on DOY 115. (d)–(f) Nitric Oxide cooling rate values at 160 km altitudes along the four orbits shown in (a) to (c).

However, as time progressed, larger NO cooling rates penetrate more equatorward in the NH than in the SH (5.3 and 7.4 UT).

Figure 6b depicts the Tdisk difference between DOY 114 and 107 at 16:10 UT (recovery phase on DOY 114) with four SABER orbits overplotted. The pink circle orbit overlapping with the GOLD FOR represents the latitude-longitude range 29°N, 10°E to 28°S, 105°W at ~8.8–9.2 (~9) UT on DOY 114. The Plus sign orbit stands for 10.5–11 (~10.8) UT and covers 57°N, 16°W to 52°S, 83°W. The star orbit (60°N, 42°W to 50°S, 90°W) represents 12.1–12.8 (~12.5) UT, and the Cross orbit (60°N, 65°W to 45°S, 98°W) stands for the 13.5–13.9 (~13.7) UT. As illustrated in Figure 6e, NO cooling rates at 160 km in the NH are the strongest near 45°N at 9 and 10.8 UT. Although the magnitude drops at 12.5 and 13.7 UT compared with 9 and 10.8 UT, its value is still strong (a maximum of $4.3 \times 10^{-7}$/erg/cm$^3$/s). In the SH, NO cooling rate > $2 \times 10^{-7}$/erg/cm$^3$/s penetrates up to 15°S at 10.8 UT (prior to storm ending at 12 UT on DOY 114). However, it drops rapidly at 12.5 and 13.7 UT (recovery phase). Nitric Oxide cooling rate > $2 \times 10^{-7}$/erg/cm$^3$/s shrinks southward to below 45°S. Overall, the changes of NO cooling rate at these four orbits illustrate that immediately after the storms (within 2 hr) there is stronger NO cooling in the NH portion of GOLD FOR persists longer than that in the SH.

Figure 6c shows the Tdisk difference between DOY 115 and 107 at 12:10 UT (recovery phase on DOY 115) with four orbits overplotted. The pink circle that overlapped with GOLD FOR stands for the ~5.2–5.8 (~5.5) UT on DOY 115. The Plus sign stands for 7–8.2 (~7.6) UT. The Star stands for 9–9.8 (~9.4) UT and the Cross stands for the 10.7–11.4 (~11.1) UT. As shown in Figure 6f, compared with DOY 114, NO cooling rate at 160 km is much smaller (mostly less than $2 \times 10^{-7}$/erg/cm$^3$/s). However, NO cooling rate in the NH is 20%–30% larger than in the SH along these four orbits within the GOLD FOR. At 11.1 UT, the maximum NO cooling rate occurs at 38°N. These observations illustrate that although NO cooling rates decrease significantly within the GOLD FOR on the day after the storm, the NH continues to exhibit stronger NO cooling than the SH.

## 4. Discussion

### 4.1. $\sum O/N_2$ Response and Recovery

The $\sum O/N_2$ depletion pattern during the storm on DOY 114 (24 April) is consistent with the prediction of the classical theory of thermospheric composition responses to geomagnetic storm (Prölss, 2011). As in the classical theory the depletion has more equatorward extension and a larger magnitude in the longitude ranges with the magnetic pole (71°W in NH and 135°E in SH). Notably, during this storm, $\sum O/N_2$ depletion also occurs in the SH

within GOLD's FOR. This was not observed during previously reported weaker geomagnetic disturbances (Cai et al., 2020, 2021, 2022, 2024; Kp maximum $\leq 5$) due to the asymmetry of geomagnetic pole locations. In the SH, GOLD's FOR is further away from the magnetic pole. However, the maximum Kp of this storm is $8^+$, producing stronger equatorward and westward winds that transport the depletion into the GOLD's FOR in the SH.

The slower recovery of the NH depletion than the southern one after 12 UT on DOY 114 when the storm ends (Figure 2d) can be attributed to the fact that the NH depletion region in GOLD FOR is closer to the NH auroral oval. After 12 UT, IMF $B_z$ turns northward and the energy input decreases. The Joule heating from the magnetosphere occurs mainly near the auroral oval. Thus, the north American region, which is in GOLD's FOR, has sustained, albeit small, energy inputs to maintain the storm-induced composition perturbations, whereas in the SH, the region within GOLD's FOR is further away from the SH auroral oval and thus recovers faster.

### 4.2. Tdisk Response and Recovery

According to Killeen et al. (1997), the variation of thermospheric temperature results from a combination of solar radiation heating, Joule heating, heat conduction, horizontal and vertical heat advection, heating from chemical reactions, adiabatic heating/cooling and radiative cooling due to NO and carbon dioxide ($CO_2$). The total temperature responses driven by these processes are not instantaneous but rather an accumulated effect over time. Note that our focus is on the middle thermosphere (140–200 km) temperature; consequently, the $CO_2$ cooling will not be considered since its major contributions occur below 100 km (Killeen et al., 1997). As the storm commences, a substantial amount of solar wind energy is transferred into the upper atmosphere at high latitudes. The increased ion-neutral collisions and particle precipitation during storm events result in enhanced Joule heating, which subsequently increases the temperature of the upper atmosphere around the auroral oval. The temperature changes alter the pressure gradient, which generates the convergence and divergence of horizontal winds to cause the adiabatic heating and cooling. Moreover, both horizontal and vertical heat advection play a role, as storm-time changes in temperature and neutral winds alter the corresponding temperature gradients.

During the storm time with persistent magnetospheric energy input into the thermosphere, temperature enhancement generally dominates over cooling within the GOLD FOR, as shown in Figure 3b (10:10 UT on DOY 114). Within and near the GOLD FOR, although NO cooling observed by SABER (Figure 6d) is the largest near 45°N and 50°S (5.5 and 9 UT), the substantial energy input from Joule heating at high latitudes largely counteracts its cooling effect, sustaining elevated temperatures. In contrast, at mid-to-low latitudes far from direct Joule heating, the primary heating mechanism is adiabatic heating associated with storm-driven equatorward winds (Burns et al., 1995). However, this process is less effective at overcoming NO radiative cooling compared to Joule heating at higher latitudes, leading to comparatively smaller temperature enhancements. As shown in Figure 3b, the maximum Tdisk enhancements decline from over 300 K near 45°–60°N/S to ∼40 K near the equator.

IMF $B_z$ turned northward after 12 UT on DOY 114 (Figure 1d), indicating the end of the storm and a significant reduction of energy input to the thermosphere. Consequently, the primary heating source (Joule heating) is significantly weakened. The NO cooling rate is positively correlated with both neutral temperature and NO number density, and it varies exponentially with temperature (Wang et al., 2022). Therefore, immediately after the storm, the NO cooling rate and Tdisk are expected to reach their highest values since the storm began, which hints that NO cooling may dominate over other heating and cooling processes. However, due to observational limitations, previous studies have been unable to directly verify this theoretically hypothesized dominance in the middle thermosphere. In this study, we overcome this challenge by performing correlation analysis between NO cooling and Tdisk variations, providing first observational evidence of this correlation. Figure 7a depicts the Tdisk difference between 14:10 and 12:10 UT on DOY 114, which illustrates the Tdisk variations immediately after the storm. The SABER orbits overlapping with the GOLD FOR orbits are around 12.5 UT and 13.7 UT, the closest available UTs near 12:10 and 14:10 UT. Figure 7b shows the Tdisk difference along the two orbits and the NO cooling rates at 160 km along the orbits. We calculated the correlation coefficient between Tdisk differences along the SABER orbit and the NO cooling rates. The correlation coefficient between Tdisk difference at 14:10 and 12:10 UT and the NO cooling rate at 160 km near 12.5 UT and 13.7 UT are −0.8 and −0.4, respectively. A correlation coefficient of −0.8 indicates a strong negative relationship, meaning that a higher NO cooling rate is associated with a more negative Tdisk difference, confirming that NO cooling plays a dominant role in middle thermospheric temperature variations immediately after the storm. Interestingly, 1–2 hr after the storm (13.7 UT), the correlation between NO cooling rate and Tdisk difference drops rapidly. This suggests that as temperature

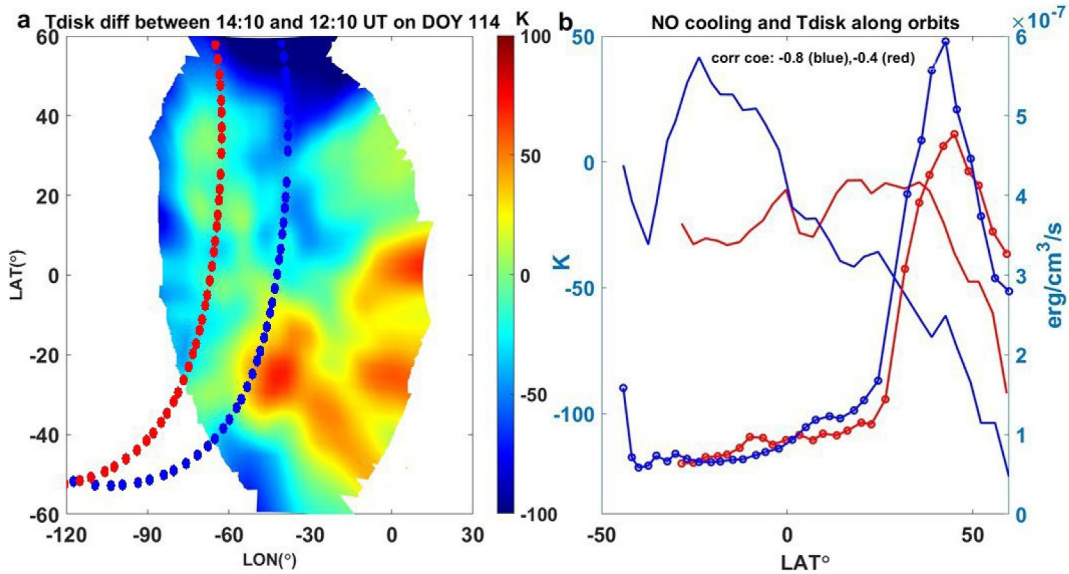


**Figure 7.** (a) Tdisk difference between 14:10 and 12:10 Universal time (UT) on DOY 114 overplotted with Nitric Oxide (NO) cooling at 12.5 UT and 13.7 UT. (b) Tdisk difference along the orbit and the NO cooling rate. Blue (solid line: Tdisk difference; solid-dot line: NO cooling) stands for NO cooling rate at 12.5 UT. Red (solid line: Tdisk difference; solid-dot line: NO cooling) stands for 13.7 UT.

continues to decrease, NO cooling becomes less significant compared to other processes. Note that the actual NO cooling variations are not fully captured by a Low-Earth-Orbiting satellite due to limitations in cross-track observations. However, despite being derived from along-track orbits, our correlation analysis remains valuable, as it provides direct observational evidence of the relationship between NO cooling and Tdisk variations immediately after the storm.

However, there is still a small amount of magnetospheric energy input near the auroral oval even after the storm ends. Note that strong NO cooling (Figures 5a–5c, 7b–7d) moves even further away from high latitudes after 12 UT on DOY 114. As a result, Tdisk enhancement formed during the storm near the auroral oval is more easily to maintain, such as in the area between 40°N and 60°N, 95°W and 25°W, as shown in Figure 3d. However, in other areas farther away from the auroral oval within the GOLD FOR, heating is more effectively offset by cooling processes. The cooling process after the storm involves multiple mechanisms. Nitric Oxide cooling remains a key contributor, though its influence is less dominant than immediately after the storm (Figure 7). Additionally, heat conduction contributes to cooling by transferring heat from hotter regions at higher altitudes to cooler regions below. Horizontal and vertical advection also play roles in modulating the cooling process. As storm-driven equatorward winds weaken after the storm, the adiabatic heating effect diminishes. Furthermore, the decreased solar irradiance during the disturbed period contributes by reducing overall solar heating of the thermosphere. Compared to quiet time (DOY 107), solar irradiance drops by approximately 11% (Qeuv from 3.4 erg/cm$^2$/s on DOY 107 to 2.94 erg/cm$^2$/s on DOY 114), directly impacting energy absorption in the upper atmosphere. As shown in Figure 3d, cooling is greater east of 50°W (within GOLD FOR), resulting in lower Tdisk than on DOY 107 4 hr after storm ends. This suggests that the accumulated effect of NO radiative cooling, in combination with reduced adiabatic heating, heat conduction and decreased solar irradiance leads to a substantial temperature drop in these regions. On the other hand, cooling and heating effects are more balanced between 100°W and 50°W, 35°N and 60°S, leading to a nearly recovered Tdisk. This balance is likely to be due to a combination of weaker NO cooling, weaker heating from high-latitudes during recovery, and continued dynamical influences such as horizontal heat advection.

On the day after the storm (DOY 115), Tdisk across almost the entire GOLD FOR is significantly lower by approximately 50–110 K—compared to DOY 107. As shown in Figures 4c, 4d and 4g–4h, the Tdisk difference between DOY 116 and 107 at NH mid-high latitudes (30°–60°N) on the following day (DOY 116) is 50–100 K higher than the difference between DOY 115 and 107, despite solar irradiance remaining similar between DOY 115 and 116. Thus, the decreasing solar irradiance from DOY 107 to 115 ($Q_{EUV}$ dropping 13%) shall play a minor

role in the lower Tdisk at NH mid-high latitudes on DOY 115 than on DOY 107. While reduced solar irradiance contributes to thermospheric cooling by decreasing overall solar heating, its effect is expected to be more pronounced at low latitudes, where direct solar heating plays a dominant role in temperature regulation. Moreover, as shown in Figure 6f, although observed maximum value of NO cooling rate drops slowly from $3.5 \times 10^{-7}$/erg/cm$^3$/s at 5.5 UT on DOY 115 to $2.2 \times 10^{-7}$/erg/cm$^3$/s at 11.05 UT within the GOLD FOR, the NH NO cooling rates are still much larger than the ones in the SH ($<1 \times 10^{-7}$/erg/cm$^3$/s). The persist strong NO cooling within the GOLD FOR shall play a major role in the lower Tdisk on DOY 115 in the NH mid-high latitudes. Note that the variations observed along the orbits provide only limited information on NO cooling. For other areas within GOLD FOR, NO cooling rate is much smaller than NH mid-high latitudes. The decreased solar irradiance, heat conduction, adiabatic cooling and NO cooling to result in the lower Tdisk. Model simulations will be used to study the roles of these processes on middle thermosphere temperature variations in the future.

## 5. Conclusion

We present the temporal evolution of the latitude-longitude distribution of thermospheric composition and neutral temperature responses to a strong geomagnetic storm (a maximum Kp of $8^+$) that occurred from 23 to 24 April in 2023. Our findings are as follows.

1. Middle thermosphere (~140–200 km) Tdisk is increased during the storm with a maximum enhancement of 340 K. The storm ends at 12 UT on DOY 114, The storm ends at 12 UT on DOY 114, and 4 hr later, lower Tdisk than the pre-storm quiet day (DOY 107) appears in the mid-low latitudes on the east side of GOLD FOR (40°N–30°S, 50°W–20°W). On the contrast, Tdisk enhancements persist in the high latitudes between 12 and 18 UT on DOY 114.
2. On the day after the storm (DOY 115), NH mid-high latitude Tdisk is 50–110 K lower than DOY 107 and is lower than the following day (DOY 116) with similar solar irradiance.
3. Correlation analysis indicates that the NO cooling rate at 160 km dominates Tdisk variation in the first 1–2 hr after the storm ends. However, this influence diminishes over time and ceases to be the primary driver of Tdisk variation as other processes take over.
4. On the day after the storm (DOY 115), NO cooling rate is stronger in the NH than in the SH, which presumably plays a crucial role in the lower Tdisk on DOY 115 at mid-high latitudes in the NH.
5. After the storm ends on DOY 114, the SH $\sum O/N_2$ depletion recovers more quickly than the NH depletion. On DOY 115, the $\sum O/N_2$ in both hemispheres have mostly recovered (percentage difference <10%).

Our study provides, for the first time, direct observational evidence of lower temperature in the middle thermosphere (140–200 km) during the storm recovery phase compared to the pre-storm quiet times, possibly as a result of the storm-time changes in NO cooling. Future research will be carried out to uncover the separate role of NO cooling and solar irradiance on the middle thermosphere temperature variations during and after a storm.

## Data Availability Statement

The GOLD data is from https://cdaweb.gsfc.nasa.gov/cgi-bin/eval1.cgi. The SABER data is from https://data.gats-inc.com/saber/Version2_0/SABER_cooling/. The Kp and F10.7 are from https://omniweb.gsfc.nasa.gov/form/dx1.html.

IMF data are from https://cdaweb.gsfc.nasa.gov/index.html.

**Acknowledgments**
This study is supported by NASA contract 80GSFC18C0061 to the University of Colorado. This work is also supported in part by NSF Grants AGS-2437053, NASA Grants NNX15AB83G, NNX17AI42G, NNX16AH06G, 80NSSC19K0278, 80NSSC18K0648, 80NSSC19K0835, NNH18ZDA001N, 80NSSC17K0013, 80NSSC22M0163, 80NSSC20K0356 and by the NASA DRIVE Science Center for Geospace Storms (CGS) under award 80NSSC22M0163.

## References

Aa, E., Zhang, S.-R., Zou, S., Wang, W., Wang, Z., Cai, X., et al. (2024). Significant midlatitude bubble-like ionospheric super-depletion structure (BLISS) and dynamic variation of storm-enhanced density plume during the 23 April 2023 geomagnetic storm. *Space Weather*, *22*(3), e2023SW003704. https://doi.org/10.1029/2023SW003704

Aksnes, A., Eastes, R., Budzien, S., & Dymond, K. (2006). Neutral temperatures in the lower thermosphere from N2 Lyman-Birge-Hopfield (LBH) band profiles. *Geophysical Research Letters*, *33*(15), L15103. https://doi.org/10.1029/2006GL026255

Burns, A. G., Killeen, T. L., Deng, W., Carignan, G. R., & Roble, R. G. (1995). Geomagnetic storm effects in the low-middle latitude upper thermosphere. *Journal of Geophysical Research*, *100*(A8), 14673–14691. https://doi.org/10.1029/94JA03232

Burns, A. G., Killeen, T. L., & Roble, R. G. (1989). Processes responsible for the compositional structure of the thermosphere. *Journal of Geophysical Research*, *94*(A4), 3670–3686. https://doi.org/10.1029/ja094ia04p03670

Burns, A. G., Killeen, T. L., & Roble, R. G. (1992). Thermospheric heating away from the auroral oval during geomagnetic storms. *Canadian Journal of Physics*, *70*(7), 544–552. https://doi.org/10.1139/p92-089

Cai, X., Burns, A. G., Wang, W., Qian, L., Solomon, S. C., Eastes, R. W., et al. (2020). The two-dimensional evolution of thermospheric ΣO/N2 response to weak geomagnetic activity during solar-minimum observed by GOLD. *Geophysical Research Letters*, *47*(18), e2020GL088838. https://doi.org/10.1029/2020GL088838

Cai, X., Burns, A. G., Wang, W., Qian, L., Solomon, S. C., Eastes, R. W., et al. (2021). Investigation of a neutral "tongue" observed by GOLD during the geomagnetic storm on May 11, 2019. *Journal of Geophysical Research: Space Physics*, *126*(6), e2020JA028817. https://doi.org/10.1029/2020JA028817

Cai, X., Wang, W., Burns, A., Qian, L., & Eastes, R. W. (2022). The effects of IMF $B_y$ on the middle thermosphere during a geomagnetically "quiet" period at solar minimum. *Journal of Geophysical Research: Space Physics*, *127*(5), e2021JA029816. https://doi.org/10.1029/2021JA029816

Cai, X., Wang, W., Eastes, R. W., Qian, L., Correira, J., & McClintock, W. E. (2024). Investigation of different ΣO/N2 variations observed by GOLD during a minor geomagnetic storm from 2 to 4 August 2021. *Journal of Geophysical Research: Space Physics*, *129*(1), e2023JA031782. https://doi.org/10.1029/2023JA031782

Cai, X., Wang, W., Lin, D., Eastes, R. W., Qian, L., Zhu, Q., et al. (2023). Investigation of the Southern Hemisphere mid-high latitude thermospheric $\sum O/N_2$ responses to the Space-X storm. *Journal of Geophysical Research: Space Physics*, *128*(3), e2022JA031002. https://doi.org/10.1029/2022JA031002

Correira, J., Evans, J. S., Lumpe, J. D., Krywonos, A., Daniell, R., Veibell, V., et al. (2021). Thermospheric composition and solar EUV flux from the Global-scale Observations of the Limb and Disk (GOLD) mission. *Journal of Geophysical Research: Space Physics*, *126*(12), e2021JA029517. https://doi.org/10.1029/2021JA029517

Eastes, R. W., McClintock, W. E., Burns, A. G., Anderson, D. N., Andersson, L., Aryal, S., et al. (2020). Initial observations by the Global-scale Observations of the Limb and Disk (GOLD) mission. *Journal of Geophysical Research: Space Physics*, *125*(7), e2020JA027823. https://doi.org/10.1029/2020JA027823

Eastes, R. W., McClintock, W. E., Burns, A. G., Anderson, D. N., Andersson, L., Codrescu, M., et al. (2017). The Global-scale Observations of the Limb and Disk (GOLD) mission. *Space Science Reviews*, *212*(1–2), 383–408. https://doi.org/10.1007/s11214-017-0392-2

Esplin, R., Mlynczak, M. G., Russell, J., & Gordley, L., & The SABER Team. (2023). Sounding of the Atmosphere using Broadband Emission Radiometry (SABER): Instrument and science measurement description. *Earth and Space Science*, *10*(9), e2023EA002999. https://doi.org/10.1029/2023EA002999

Evans, J. S., Lumpe, J. D., Eastes, R. W., Correira, J., Aryal, S., Laskar, F., et al. (2024). Disk images of neutral temperature from the Global-scale Observations of the Limb and Disk (GOLD) mission. *Journal of Geophysical Research: Space Physics*, *129*(6), e2024JA032424. https://doi.org/10.1029/2024JA032424

Evans, J. S., Strickland, D. J., & Huffman, R. E. (1995). Satellite remote sensing of thermospheric O/N2 and solar EUV: 2. Data analysis. *Journal of Geophysical Research*, *100*(A7), 12227–12233. https://doi.org/10.1029/95ja00573

Fuller-Rowell, T. J., Codrescu, M. V., Moffett, R. J., & Quegan, S. (1994). Response of the thermosphere and ionosphere to geomagnetic storms. *Journal of Geophysical Research*, *99*(A3), 3893–3914. https://doi.org/10.1029/93ja02015

Killeen, T. L., Burns, A. G., Azeem, I., Cochran, S., & Roble, R. G. (1997). A theoretical analysis of the energy budget in the lower thermosphere. *Journal of Atmospheric and Solar-Terrestrial Physics*, *59*(6), 675–689. https://doi.org/10.1016/s1364-6826(96)00114-9

Knipp, D. E., Kilcommons, L., Hunt, L., Mlynczak, M., Pilipenko, V., Bowman, B., et al. (2013). Thermospheric overcooling response to sheath driven Geospace storms. *Geophysical Research Letters*, *40*(7), 1263–1267. https://doi.org/10.1002/grl.50197

Knipp, D. J., Pette, K., Isaacs, F., Cruz, M. M., & Hunt, L. A. (2017). Nitric Oxide: Thermospheric nitric oxide response to shock led-storms. *Space Weather*, *15*, 325–342. https://doi.org/10.1002/2016SW001567

Lei, J., Burns, A. G., Thayer, J. P., Wang, W., Mlynczak, M. G., Hunt, L. A., et al. (2012). Overcooling in the upper thermosphere during the recovery phase of the 2003 October storms. *Journal of Geophysical Research*, *117*(A3), A03314. https://doi.org/10.1029/2011JA016994

Lei, J., Thayer, J. P., Lu, G., Burns, A. G., Wang, W., Sutton, E. K., & Emery, B. A. (2011). Rapid recovery of thermosphere density during the October 2003 geomagnetic storms. *Journal of Geophysical Research*, *116*(A3), A03306. https://doi.org/10.1029/2010JA016164

Li, J., Wang, W., Lu, J., Yuan, T., Yue, J., Liu, X., et al. (2018). On the responses of mesosphere and lower thermosphere temperatures to geomagnetic storms at low and middle latitudes. *Geophysical Research Letters*, *45*(19), 10128–10137. https://doi.org/10.1029/2018GL078968

Li, S., Ren, Z., Yu, T., Chen, G., Li, G., Zhao, B., et al. (2024). The daytime variations of thermospheric temperature and neutral density over Beijing during minor geomagnetic storm on 3–4 February 2022. *Space Weather*, *22*(2), e2023SW003677. https://doi.org/10.1029/2023SW003677

Li, S., Ren, Z., Yu, T., Li, G., Yue, X., Liu, L., et al. (2025). Variations in the thermosphere during the 2018 SSW event at Beijing and Wuhan. *Journal of Geophysical Research: Space Physics*, *130*, e2025JA033767. https://doi.org/10.1029/2025JA033767

Liu, X., Yue, J., Wang, W., Xu, J., Zhang, Y., Li, J., et al. (2018). Responses of lower thermospheric temperature to the 2013 St. Patrick's Day geomagnetic storm. *Geophysical Research Letters*, *45*(10), 4656–4664. https://doi.org/10.1029/2018GL078039

Mlynczak, M., Martin-Torres, F. J., Russell, J., Beaumont, K., Jacobson, S., Kozyra, J., et al. (2003). The natural thermostat of nitric oxide emission at 5.3 μm in the thermosphere observed during the solar storms of April 2002. *Geophysical Research Letters*, *30*(21), 2100. https://doi.org/10.1029/2003GL017693

Mlynczak, M. G. (1997). Energetics of the mesosphere and lower thermosphere and the SABER experiment. *Advances in Space Research*, *20*(6), 1177–1183. https://doi.org/10.1016/S0273-1177(97)00769-2

Mlynczak, M. G., Hunt, L. A., Lopez-Puertas, M., Funke, B., Emmert, J., Solomon, S., et al. (2021). Spectroscopy, gas kinetics, and opacity of thermospheric nitric oxide and implications for analysis of SABER infrared emission measurements at 5.3 μm. *Journal of Quantitative Spectroscopy and Radiative Transfer*, *268*, 107609. https://doi.org/10.1016/j.jqsrt.2021.107609

Mlynczak, M. G., Hunt, L. A., Marshall, B. T., Martin-Torres, F. J., Mertens, C. J., Russell, J. M., et al. (2010). Observations of infrared radiative cooling in the thermosphere on daily to multiyear timescales from the TIMED/SABER instrument. *Journal of Geophysical Research*, *115*(A3), A03309. https://doi.org/10.1029/2009JA014713

Mlynczak, M. G., Martin-Torres, F. J., Crowley, G., Kratz, D. P., Funke, B., Lu, G., et al. (2005). Energy transport in the thermosphere during the solar storms of April 2002. *Journal of Geophysical Research*, *110*(A12), A12S25. https://doi.org/10.1029/2005JA011141

Mlynczak, M. G., Martin-Torres, F. J., & Russell, J. M. (2007). Correction to "Energy transport in the thermosphere during the solar storms of April 2002". *Journal of Geophysical Research*, *112*(A2), A02303. https://doi.org/10.1029/2006JA012008

Pancheva, D., Singer, W., & Mukhtarov, P. (2007). Regional response of the mesosphere-lower thermosphere dynamics over Scandinavia to solar proton events and geomagnetic storms in late October 2003. *Journal of Atmospheric and Terrestrial Physics*, *69*(9), 1075–1094. https://doi.org/10.1016/j.jastp.2007.04.005

Paxton, L. J., Strickland, D. J., Humm, D. C., Christensen, A. B., Ogorzalek, B. S., Pardoe, C. T., et al. (1999). Global ultraviolet imager (GUVI): Measuring composition and energy inputs for the NASA Thermosphere Ionosphere Mesosphere Energetics and Dynamics (TIMED) mission. In *Proceedings of SPIE* (Vol. 3756, pp. 265–276). https://doi.org/10.1117/12.366380

Prölss, G. W. (2011). Density perturbations in the upper atmosphere caused by the dissipation of solar wind energy. *Surveys in Geophysics*, *32*(2), 101–195. https://doi.org/10.1007/s10712-010-9104-0

Russell, J., Mlynczak, M., Gordley, L., Tansock, J., & Esplin, R. (1999). An overview of the SABER experiment and preliminary calibration results. *Proceedings of SPIE*, *3756*, 277–288. https://doi.org/10.1117/12.366382

Sheng, C., Lu, G., Solomon, S. C., Wang, W., Doornbos, E., Hunt, L. A., & Mlynczak, M. G. (2017). Thermospheric recovery during the 5 April 2010 geomagnetic storm. *Journal of Geophysical Research: Space Physics*, *122*(4), 4588–4599. https://doi.org/10.1002/2016JA023520

Strickland, D. J., Evans, J. S., & Paxton, L. (1995). Satellite remote sensing of thermospheric $O/N_2$ and solar EUV: 1. Theory. *Journal of Geophysical Research*, *100*(A7), 12217–12226. https://doi.org/10.1029/95JA00574

Strickland, D. J., Lean, J. L., Meier, R. R., Christensen, A. B., Paxton, L. J., Morrison, D., et al. (2004). Solar EUV irradiance variability derived from terrestrial far ultraviolet dayglow observations. *Geophysical Research Letters*, *31*(3), L03401. https://doi.org/10.1029/2003GL018415

Verkhoglyadova, O. P., Mannucci, A. J., Tsuratani, B. T., Mlynczak, M. G., Hunt, L. A., & Redmon, R. (2014). Localized thermosphere ionization events during the high speed stream interval of 29 April - 5 May 2011. *J. Geophys. Res.Space Physics, Space Physics*, *120*, 675–696. https://doi.org/10.1002/2014JA020535

Verkhoglyadova, O. P., Meng, X., Mannucci, A. J., Mlynczak, M. G., Hunt, L. A., & Lu, G. (2017). Estimation of ionosphere-thermosphere energy budget for ICME storms of March 2013 and 2015 with GITM and observational proxies. *Space Weather*, *15*(9), 1102–1124. https://doi.org/10.1002/2017SW001650

Wang, N., Mlynczak, M. G., Emmert, J. T., Lopez-Puertas, M., & Funke, B. (2024). Nitric oxide concentration: A new data set derived from SABER measurements. *Earth and Space Science*, *11*(5), e2023EA003252. https://doi.org/10.1029/2023EA003252

Wang, N., Yu, W., Yue, J., Wang, W., Qian, L., Mclnerney, J. M., et al. (2022). Thermospheric nitric oxide cooling responses to the 14 December 2020 solar eclipse. *Journal of Geophysical Research: Space Physics*, *127*(12), e2022JA030995. https://doi.org/10.1029/2022JA030995

Wang, N., Yue, J., Wang, W., Qian, L., Jian, L., & Zhang, J. (2021). A comparison of the CIR- and CME-induced geomagnetic activity effects on mesosphere and lower thermospheric temperature. *Journal of Geophysical Research: Space Physics*, *126*(6), 1–15. https://doi.org/10.1029/2020ja029029

Yu, T., Cai, X., Ren, Z., Li, S., Pedatella, N., & He, M. (2022a). Investigation of the $\Sigma O/N_2$ depletion with latitudinally tilted equatorward boundary observed by GOLD during the geomagnetic storm on April 20, 2020. *Journal of Geophysical Research: Space Physics*, *127*(12), e2022JA030889. https://doi.org/10.1029/2022JA030889

Yu, T., Cai, X., Ren, Z., Wang, Z., Pedatella, N. M., & Jin, Y. (2023). Investigation of interhemispheric asymmetry of the thermospheric composition observed by GOLD during the first strong geomagnetic storm in solar-cycle 25, 1: IMF By effects. *Journal of Geophysical Research: Space Physics*, *128*, e2023JA031429. https://doi.org/10.1029/2023JA031429

Yu, T., Wang, W., Ren, Z., Cai, X., & He, M. (2023). Vertical variations in thermospheric $O/N_2$ and the relationship between O and $N_2$ perturbations during a geomagnetic storm. *Earth and Space Science*, *10*, e2023EA002988. https://doi.org/10.1029/2023EA002988

Yu, T., Wang, W., Ren, Z., Cai, X., Liu, L., He, M., et al. (2022b). Diagnostic analysis of the physical processes underlying the long-duration $\Sigma O/N_2$ depletion during the recovery phase of the 8 June 2019 geomagnetic storm. *Journal of Geophysical Research: Space Physics*, *127*(12), e2022JA031075. https://doi.org/10.1029/2022JA031075

Yu, T., Wang, W., Ren, Z., Cai, X., Yue, X., & He, M. (2021). The response of middle thermosphere (~160 km) composition to the November 20 and 21, 2003 superstorm. *Journal of Geophysical Research: Space Physics*, *126*(10), e2021JA029449. https://doi.org/10.1029/2021JA029449

Yuan, T., Zhang, Y., Cai, X., She, C.-Y., & Paxton, L. J. (2015). Impacts of CME-induced geomagnetic storms on the midlatitude mesosphere and lower thermosphere observed by a sodium lidar and TIMED/GUVI. *Geophysical Research Letters*, *42*(18), 7295–7302. https://doi.org/10.1002/2015GL064860

Zhang, Y., Paxton, L. J., Lu, G., & Yee, S. (2019). Impact of nitric oxide, solar EUV and particle precipitation on thermospheric density decrease. *Journal of Atmospheric and Solar-Terrestrial Physics*, *182*, 147–154. https://doi.org/10.1016/j.jastp.2018.11.016